Near-field Inductive Coupling Link To Power a Three-Dimensional Millimeter-Size Antenna for Brain Implantable Medical Devices

Article *in* IEEE Transactions on Biomedical Engineering · November 2017

DOI: 10.1109/TBME.2017.2778729

CITATIONS
10

READS
296

5 authors, including:

Mohamed Manoufali
The University of Queensland
25 PUBLICATIONS **76** CITATIONS
SEE PROFILE

Konstanty S Bialkowski
The University of Queensland
120 PUBLICATIONS **604** CITATIONS
SEE PROFILE

Beadaa Jasem Mohammed
The University of Queensland
32 PUBLICATIONS **439** CITATIONS
SEE PROFILE

Paul C Mills
The University of Queensland
229 PUBLICATIONS **2,706** CITATIONS
SEE PROFILE

Near-Field Inductive-Coupling Link to Power a Three-Dimensional Millimeter-Size Antenna for Brain Implantable Medical Devices

Mohamed Manoufali, *Student Member, IEEE*, Konstanty Bialkowski, *Member, IEEE*, Beadaa Jasem Mohammed, *Member, IEEE*, Paul C. Mills, and Amin Abbosh, *Senior Member, IEEE*

Abstract*—*Objective: **Near-field inductive-coupling link can establish a reliable power source to a *batteryless* implantable medical device based on Faraday's law of induction. *Methods:* In this paper, the design, modeling, and experimental verification of an inductive-coupling link between an off-body loop antenna and a 0.9 mm^3 three-dimensional (3-D) bowtie brain implantable antenna is presented. To ensure reliability of the design, the implantable antenna is embedded in the cerebral spinal fluid of a realistic human head model. Exposure, temperature, and propagation simulations of the near electromagnetic fields in a frequency-dispersive head model were carried out to comply with the IEEE safety standards. Concertedly, a fabrication process for the implantable antenna is proposed, which can be extended to devise and miniaturize different 3-D geometric shapes. *Results:* The performance of the proposed inductive link was tested in a biological environment; *in vitro* measurements of the fabricated prototypes were carried in a pig's head and piglet. The measurements of the link gain demonstrated −35.83 dB in the pig's head and −30.81 dB in piglet. *Significance:* The *in vitro* measurement results showed that the proposed 3-D implantable antenna is suitable for integration with a miniaturized *batteryless* brain implantable medical device (BIMD).**

***Index Terms*—Inductive coupling link, realistic human head model, frequency-dispersive dielectric properties, implantable antennas, near EM fields exposure and penetration.**

I. Introduction

With the growing interest in personalized healthcare systems, implantable medical devices (IMDs) have witnessed an unprecedented frontier due to advancements in biomedical technology [1], [2]. IMDs are embedded inside a patient's body surgically for tailored disease diagnosis, monitoring and treatment. The significance of implantable medical devices relies on providing continuous *in-vivo* information for pathological and physiological changes in a specific tissue over time. This *"in-close"* implantation offers flexibility and reliability in measuring the changes of a specific tissue compared to external monitors [1]. Typical applications include implantable pacemakers [3], glucose monitors [4], [5] and intracranial pressure monitors [6].

In a specific application of implantable medical devices, brain implantable medical devices (BIMDs) have a strong potential to substantially improve the welfare and quality of life of people suffering from enervating circumstances such as spinal cord injuries and limb loss. *In-vivo* BIMDs proliferate a plethora of applications spanning from restoring mobility for amputees, early detection of neurological disorders such as epilepsy, to understanding the brain's behaviors for patients with neurodegenerative diseases like Alzheimer's and Parkinson's [7], [8].

Most of BIMDs are envisaged to be embedded in the cerebral spinal fluid (CSF). CSF is a protective layer that covers the brain cortex and spine and can reflect some of the pathological and physiological changes that occur in the brain [9]. Consequently, BIMDs sense physical changes of the brain (e.g. CSF pressure, neural signals, temperature and variation of the local effective permittivity), and convert them to sensing information by an exterior reader. Despite the fact that BIMDs have been witnessing a notable progress, enabling a continuous power for the operation of a BIMD is still a main challenge [10], [11].

There are several other challenges in the actual realization of BIMDs. Particularly, from a patient's safety and comfort perspective, while providing continuous sensing, the sensing data needs to be exchanged wirelessly with an exterior reader to process the collected physical information. Furthermore, the wireless communication between an exterior reader and BIMD avoids tethered connection and limitation of a BIMD solely to a clinical setup [12].

To avail a continuous power for BIMDs while avoiding batteries, short-range near-field inductive links have been utilized for wireless power transfer to a *battery-less* BIMD [13]. Though operating in low frequencies reduces the huge losses by biological tissues, it results in large exterior antennas and low data rate [14]. As evidenced from the analytical and numerical simulations in

Manuscript received October 8, 2017; accepted November 19, 2017. Date of current version December 20, 2017. *(Corresponding author: Mohamed Manoufali.)*

M. Manoufali is with the School of Information Technology and Electrical Engineering, The University of Queensland, Brisbane, QLD 4072, Australia (e-mail: m.manoufaliu@uq.edu.au).

K. Bialkowski, B. Mohamed, and A. Abbosh are with the School of Information Technology and Electrical Engineering, The University of Queensland.

P. C. Mills is with the School of Veterinary Science, The University of Queensland.

Digital Object Identifier 10.1109/TBME.2017.2778729

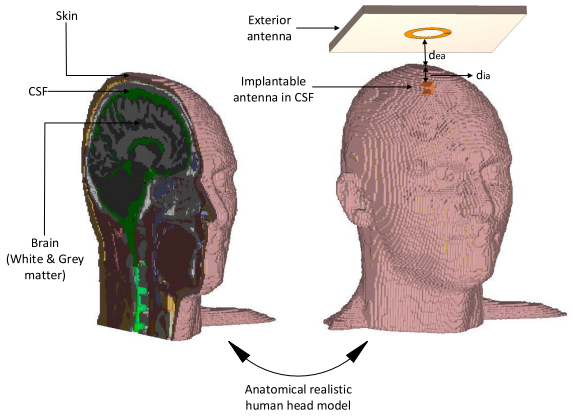

Fig. 1. A wireless power link between an exterior antenna inductively coupled to an implantable antenna in CSF of a realistic human head model.

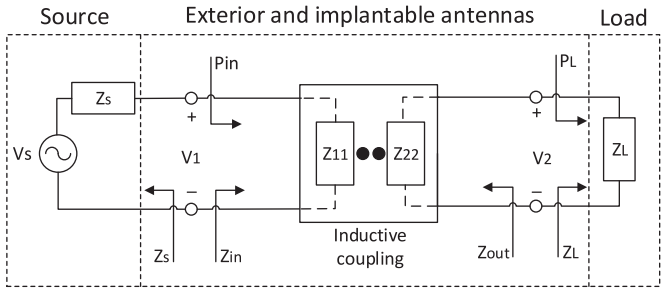

Fig. 2. Two-port network of the wireless link through human head tissues between the exterior and implantable antennas.

[15], for mm-size implantable antennas, sub GHz and low GHz range provide the optimal frequency to maximize the link gain depending on the dimension of the exterior antenna. Therefore, higher frequencies such as medical implant communication system (MICS) band (402–405 MHz) is utilized in the literature to overcome the drawbacks of a low frequency wireless link between an exterior reader and BIMD. This exclusively allocated band for medical implants poses major benefits [16], [17], which are: 1) it minimizes frequency interference problems, 2) lies in the low noise portion of the frequency spectrum 3) the same band can be used to concurrently power the BIMD and establish a communication data link but most importantly 4) it allows acceptable penetration to CSF with a link gain > -60 dB. This value is a rough estimation based on many factors such as size and type of the utilized antennas, noise level, sensitivity and dynamic range of the whole link [16], [17]. In fact, the operating frequency should represent a good compromise to obtain a compact exterior antenna, acceptable penetration in the tissues and satisfactory power transfer to a miniature *battery-less* medical device with a strong inductive coupling to the exterior reader.

In [18], an inductive coupling link is proposed for a 8 mm^3 3D cube implantable antenna coupled to an exterior copper fabric and embroidered loop antennas. The link is designed at 300 MHz and measured in a head-equivalent liquid phantom. Likewise, in [19], a 1 mm^3 3D implantable antenna is designed and built. However, the performance of the inductive link is not investigated in a realistic environment to study the adverse effect of the biological tissues in the wireless link [19]. The measurements in [19] were restricted to free-space only and ignored the mismatch loss between the implantable antenna and the load. *In-vitro* tests of the inductive coupling link for a 1 mm^2 planar antenna is given in [20] with a simple multilayer tissue model used in the simulation. Generally, in the literature, a perfect conjugate matching is assumed between the implantable antenna and the load. This assumption does not hold when integrating the implantable antenna with a high capacitive IC [21].

In an extension to our initial efforts [22], we aim in this work at designing and experimenting, in a realistic environment, the near-field wireless power link between a 0.9 mm^3 3D bowtie brain implantable antenna and an off-body exterior loop antenna. The link is characterized based on the operating power gain (G_{op}) that takes into consideration the impedance mismatch loss (ML) unlike the maximum operating power gain ($G_{op,\max}$) presented in [18]–[20]. Numerical simulations were performed in a realistic human head model with 46 tissues to study the efficacy of the near-field inductive coupling link. Adherence to the safety requirements is investigated through the specific absorption rate (SAR), temperature distribution and the near-field propagation. The measurements of the proposed inductive link were conducted in a pig's head and piglet to verify the performance in a realistic environment. In addition, a near-field measurement of the exterior antenna is performed to investigate the lateral misalignment of the exterior antenna on the inductive coupling link.

II. Modeling of the Near-Field Wireless Power Link

The electromagnetic (EM) fields are highly affected by the dielectric properties of the biological tissues. When an implantable antenna is interrogated by an exterior antenna, the dielectric properties results in power absorption, particularly for the electric field [16]. In contrast, the magnetic response is usually very weak, since, the magnetic permeability of most tissues is equivalent to free-space $\mu = \mu_o$ [23]. For this reason, inductive coupling is a favorable method for power transfer to a *battery-less* BIMD.

The coupling is predominately achieved through magnetic fields leading to reduce the interaction of the EM fields with the surrounding biological tissues. The reading distance between the exterior antenna and the implantable antenna falls in the near-field region [24]. In Fig. 1, the wireless link between the off-body exterior antenna with a distance d_{ea} from the skin interface and implantable antenna with implantation depth d_{ia} in a realistic human head is depicted. The inductive coupling link between the exterior antenna and implantable antennas is modeled by the lossy two-port network as shown in Fig. 2.

Unlike far-field simulations, where the wireless link can be investigated separately from the antennas, the link between the exterior and implantable antennas needs to be incorporated in the simulation [20]. The metric to quantify the performance of the wireless power link is the power transfer gain, which can be defined as the operating power gain G_{op}. G_{op} is the ratio between the power delivered to the load (P_L) to the power supplied

to the exterior antenna i.e. accepted power (P_{in}). When the input impedance and output impedance are conjugately matched to the source and load respectively, the maximum operating power gain ($G_{op,\max}$) is achieved [25]. The difference between G_{op} and $G_{op,\max}$ is that the latter neglects the mismatch loss ($\mathrm{ML(dB)} = 10\log_{10}(1-|\Gamma|^2)$) between the implantable antenna and an integrated load [21]. However, in practice, fabrication inaccuracies alter the conjugate matching and impedance mismatch loss occurs. Therefore, for the rest of the analysis, G_{op} is considered to describe the wireless power link.

The operating power gain (G_{op}) and the maximum operating power gain ($G_{op,\max}$) in terms of Z parameters are given by

$$G_{op} = \frac{P_L}{P_{in}} = \frac{|Z_{21}|^2}{|Z_{22}+Z_L|^2}\frac{\Re(Z_L)}{\Re(Z_{11}-\frac{Z_{12}Z_{21}}{Z_{22}+Z_L})} \quad (1)$$

$$G_{op,\max} = \frac{|Z_{21}|^2}{M+\sqrt{M^2-|Z_{12}Z_{21}|^2}}$$
$$\text{where; } M = 2\Re(Z_{11})\Re(Z_{22}) - \Re(Z_{12}Z_{21}) \quad (2)$$

where Z_{11}, Z_{22} and Z_L represent the self-impedance of the exterior antenna, implantable antenna and load, respectively. Z_{21} and Z_{12} denote the mutual impedance between the exterior and implantable antennas.

III. Frequency-Dispersive Dielectric Properties for Realistic Human Head Model

In regard to the simulation of BIMDs, majority of the work in the literature utilizes a simple multilayer planar phantom with a limited number of tissues [26], [27]. Nonetheless, the use of an anatomical realistic human head model provides accuracy and reliability to realize BIMDs and investigate EM fields propagation in the tissues. In addition, the head model provides a platform to test the absorption and temperature distribution due to incident EM fields.

The basis of this work involves the use of a human head model that mimics the structural heterogeneity of the human head. The Duke head model [28] shown in Fig. 1 is obtained after classifying tissues by using high resolution MRI head images. The model consists of 150 transverse slices and contains $155 \times 305 \times 150$ cubics with a resolution of 2 mm yielding a total dimension of 310 mm $\times$ 610 mm $\times$ 300 mm. The human head model consists of 46 tissues and it is considered the most detailed voxel-based model available in the literature. The dielectric properties are imported for each tissue based on the dispersive frequency dependent data available in the literature [29] to CST Microwave studio [30] for a frequency range ($0.1-1$ GHz). However, in [29] the dielectric properties of some of the tissues included in our used human head model are not characterized, hence, the dielectric properties from similar tissues are taken instead as per the guidelines in [31]. Thus, the number of tissues is reduced to 20 from 46 in terms of the similar dielectric properties. The dielectric properties of human tissues are frequency dependent and the complex permittivity is

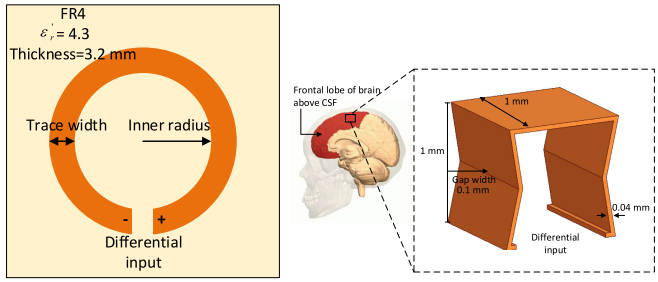

Fig. 3. Geometry of the exterior and implantable antennas (the dimensions are not in scale). (a) Exterior antenna and (b) implantable antenna embedded in the CSF above the frontal lope of the brain.

modeled using normally a fourth-order Cole-Cole model as

$$\varepsilon_r'(\omega) = \varepsilon_\infty + \sum_{i=1}^{4}\frac{\triangle\varepsilon_i}{1+(j\omega\tau_i)^{1-\alpha_i}} + \frac{\sigma}{j\omega\varepsilon_0} \quad (3)$$

The complex relative permittivity of the tissues $\varepsilon_r'(\omega)$ is expressed in the Cole-Cole model as a function of an angular frequency ω, where τ_i is the relaxation time, σ is the static conductivity. The dispersion is given by $\triangle\varepsilon_i = \varepsilon_{si} - \varepsilon_\infty$, where ε_{si} denotes the static permittivity when τ_i is much smaller than $1/\omega$.

IV. Exterior and Implantable Antennas Design

When an exterior antenna is excited, it generates a magnetic field near its vicinity. This magnetic field induces a current in the implantable antenna if it exists in the near-field of the exterior reader. Under this situation, the exterior-implantable antenna establishes an inductive coupling between flowing current in the exterior antenna and induced voltage across the implantable antenna. Maximizing the power delivered to the load in conjunction with adhering to the SAR limited by the safety standard depends on the antenna design and accepted power to the exterior antenna. The fact that SAR is directly proportional to the electric field upholds the selection of magnetic based antennas [16]. Consequently, loop antennas are utilized, since they provide a higher magnetic near-field, which helps in improving the coupling strength in the heterogeneous human head tissues.

Increasing the size of the exterior antenna assists in increasing G_{op}, thereby, delivering more power to the BIMD. However, a low profile and compact exterior antenna is desirable, since it is envisaged to be part of a wearable cap or a portable device. For the exterior antenna (Fig. 3(a)), the loop antenna is printed on the low cost FR4 laminate ($\varepsilon_r = 4.3$ and $\tan\delta = 0.025$) with a thickness of 3.2 mm and separation of $d_{ea} = 3$ mm from the skin interface. For the proposed implantable antenna (Fig. 3(b)), the 3D bowtie antenna has an inner gap width of 0.1 mm with a total volume of 0.9 mm^3 and an implantation depth of $d_{ia} = 12$ mm. The 3D antennas provide a wider coupling area compared to planar antennas with the same cross section [32]. Moreover, a rod of a high permeability ferrite material can be inserted in its cavity to increase the radiation resistance and the link gain. This

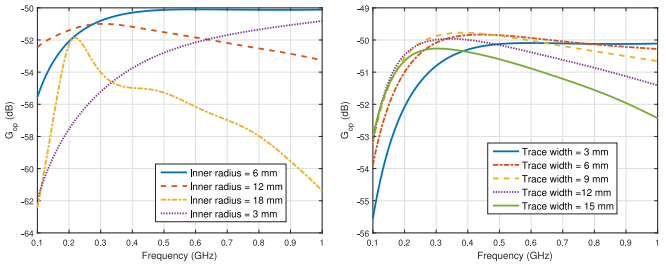

Fig. 4. Effect of changing (a) the inner radius and (b) trace width of the exterior antenna on the operating power gain (G_{op}) of the wireless link between the exterior and implantable antennas.

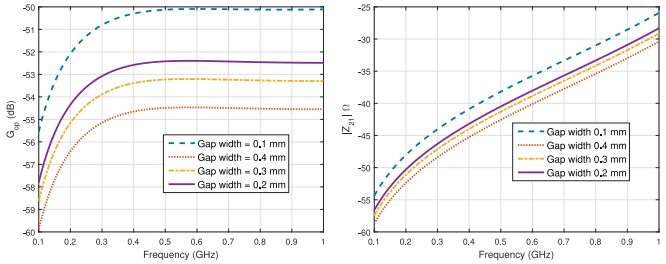

Fig. 5. Effect of changing (a) the gap width of the 3D bowtie implantable antenna on the operating power gain (G_{op}) and (b) mutual coupling strength ($|Z_{21}|$) between the exterior and implantable antennas.

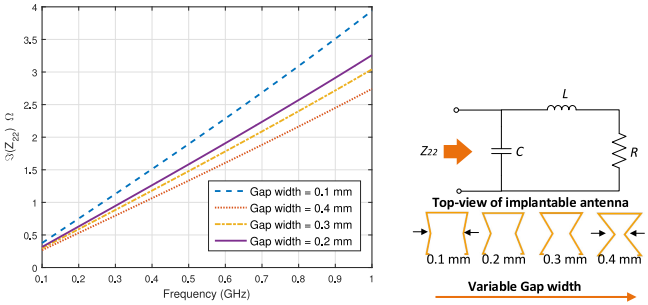

Fig. 6. Effect of changing the gap width on the reactive impedance of the implantable antenna and its equivalent lumped circuit model.

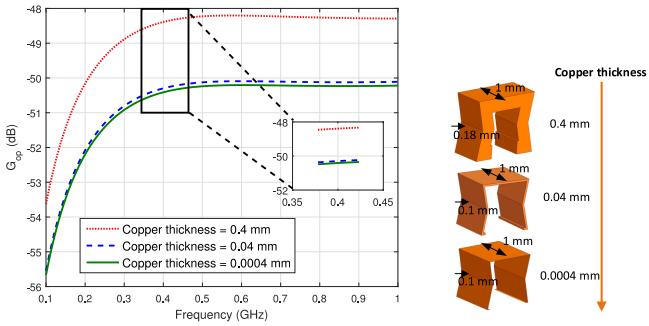

Fig. 7. Variation of the copper thickness of the implantable antenna and its effect on the operating power gain (G_{op}) of wireless link.

is known as a ferrite-loop, which has a higher magnetic flux and field compared to the conventional loop antenna [33].

In [15], the authors concluded that the operating frequency which reduces the link loss shifts down to lower frequencies, while increasing the exterior antenna size decreases the link loss. Consistently, there is an optimum exterior size that reduces the link loss at the frequency of interest (MICS band in our case). The inner radius of the exterior antenna is varied from 3 mm to 18 mm in order to find the optimum exterior antenna size while the trace width is fixed to 3 mm as shown in Fig. 4(a), while keeping the gap width of the implantable antenna to 0.1 mm, length and height of 1 mm. The results in Fig. 4(a) reaffirm that there exists an optimum exterior antenna size for the 0.9 mm^3 that reduces the link loss at the frequency of interest, increasing the exterior antenna size can lower the frequency of operation to 0.2 GHz as in the case of an inner radius of 18 mm. We also observe that the maximum operating power gain that minimizes the overall link loss to the implantable antenna occurs when the inner radius is equal to 6 mm.

The ohmic loss of the exterior antenna also affects the link loss and therefore, keeping low loss ohmic loss is desirable to maximize (G_{op}). Hence, we investigated the effect of varying the trace width of the exterior antenna while keeping the dimensions of the implantable antenna similar to the case of Fig. 4(a). As a result of increasing the trace width, the surface area of the exterior and its ohmic loss increase. From Fig. 4(b), a trace width of 3 mm has a rather broad maximum G_{op} and increasing the trace width leads to increase the link loss noticeably at higher frequencies.

At the implantable antenna, there is another parameter that influences the operating power gain, which is the gap width of the 3D bowtie antenna. For this configuration, a gap width sweep of (0.1–0.4 mm) is selected to investigate the impact on the link loss when the exterior loop inner radius and trace width are 6 mm and 3 mm, respectively, as shown in Fig. 5(a). Increasing the gap width, increases the capacitance between the inner plate and reduces the magnetic coupling strength (Z_{21}) as shown in Fig. 5(b). Due to the small size of the implantable antenna, this can be better explained using an equivalent lumped circuit model of the implantable antenna. In considering the lumped equivalent circuit of the implantable antenna shown Fig. 6, the capacitance increases with the gap width, which subsequently, reduces the inductive nature of the implantable antenna by pulling down the impedance (Z_{22}) as shown in Fig. 6.

Commonly, the loss resistance of a small loop is much larger than its radiation resistance [33]. For a mathematical simplification adopted from [33], the loss resistance of a small loop with a radius a is hypothesized to be similar to a small wire with a radius b, and given by

$$R_{ohmic} = \frac{a}{b} R_s \tag{4}$$

where R_s is the surface impedance of conductor and given by

$$R_s = \frac{1}{\sigma \delta_s} \tag{5}$$

$$\text{where; } \delta_s = \frac{1}{\sqrt{\pi f \mu \sigma}}$$

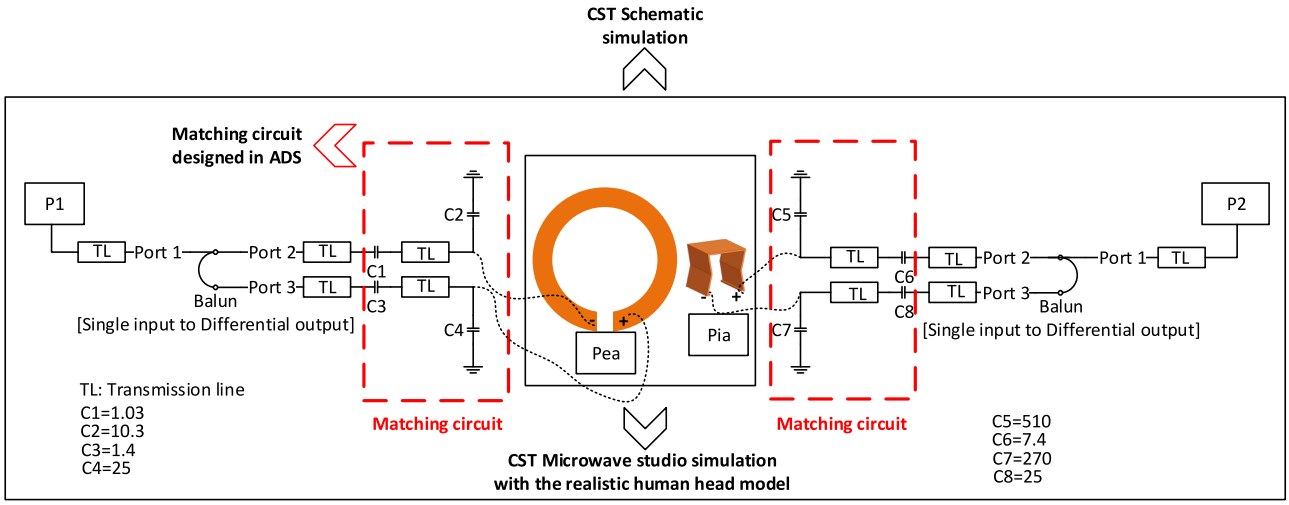

Fig. 8. Simulation setup for the two-port network, exterior and implantable antennas in CST Microwave studio (Ports $\mathrm{P_{ea}}$ and $\mathrm{P_{ia}}$) are dynamically linked to the components in CST schematic [30] (Ports P1 and P2) subsequently (the values of the used capacitors are in pF).

In microwave frequencies, the ohmic loss is affected by the skin depth (δ_s) as shown in (5). From (4), the ohmic resistance can be reduced by using a thicker or a high-conductivity conductor, which ultimately improves the link gain. At 402 MHz, the skin depth is around 0.003 mm, hence, three cases for the copper sheet thickness have been investigated namely 0.4 mm, 0.04 mm and 0.0004 mm. These three cases represent an increase by a factor of 100, 10 and a reduction by a factor of 10 for the skin depth at 402 MHz, respectively. As expected from (4)–(5), using a thick copper sheet for the implantable antenna reduces the ohmic resistance. Based on the simulation results as shown in Fig. 7, around 3 dB improvement is attained for the 0.4 mm copper thickness compared to 0.0004 mm and 0.04 mm. Nevertheless, considering the ease of fabrication and availability of a copper sheet of thickness (0.04 mm) in our lab, this has been selected for the fabrication of the implantable antenna.

As mentioned earlier, the impedance of the loop antenna has a low radiation resistance (real part) and a large reactance (imaginary part), which causes a large reflection if connected directly to a vector network analyzer (VNA) with a characteristic impedance of 50 Ω. To address that, a matching circuit is designed with a surface-mount balun (ATB2012-5001) to provide a differential feeding to the exterior and implantable antennas. From the CST Microwave studio simulation [30], S parameters between (Ports $\mathrm{P_{ea}}$ and $\mathrm{P_{ia}}$) are exported to ADS to design a matching circuit as shown in Fig. 8. Since the loop has an inductive nature, series and shunt capacitors are used to eliminate the reactive part of the input impedance and improve the radiation resistance. Furthermore, transmission lines are included with the S parameter file of the balun in the CST schematic simulation [30]. The CST schematic is dynamically linked to the CST Microwave studio simulation [31] to study the effect of the SAR, temperature distribution and 3D field propagation, when port P1 is excited with 1 W input power, while keeping port P2 as an impedance of 50 Ω, which represents the characteristic impedance of the VNA (Z_L). The dimension of the exterior antenna is optimized to maximize G_{op} in the CST Microwave studio [30] giving a simulated wireless link gain of −50.29 dB at MICS band between (Ports $\mathrm{P_{ea}}$ and $\mathrm{P_{ia}}$) in Fig. 8. After adding the transmission lines, baluns and matching circuits, an improvement of 24 dB is obtained achieving a wireless link gain of −27.87 dB between (Ports P1 and P2) in the CST Schematic [30] as shown in Fig. 8.

V. Near-Field Characterization

For the proposed exterior antenna, the maximum diameter, $2R \ll \lambda_{eff}$, where λ_{eff} denotes the effective wavelength, hence, the near-field region extends up to $\lambda_{eff}/2\pi$. Giving an operating frequency of 402 MHz and FR4 as a substrate, the near-field region can extend up to 57 mm. However, the absorption of the fields in the biological tissues impedes the penetration. Therefore, near-field simulations are conducted as shown in Fig. 9. Two simulation setups are used to characterize the near-field propagation. Firstly, to investigate the coupling with the implantable antenna, a Gaussian excitation signal from the exterior antenna is excited in CST schematic [31] and the response of the near electric (E) and magnetic fields (H) are recorded for y-oriented E and H field probes located at 5, 10, 15, 20, 25, and 30 mm from the center of the exterior loop antenna in the CST Microwave studio simulation [30] as shown in Fig. 9.

The near E and H fields at 402 MHz for the exterior antenna is shown in Fig. 10. When EM fields impinge the skin layer, the electric field is absorbed and its strength decreases as shown in Fig. 10(a), whereas, there is a smooth transition (penetration) of the magnetic field in the head Fig. 10(c). Since, the implantable antenna falls within the near-field of the exterior antenna, the magnetic field induces a current giving rise to the magnetic field as shown Fig. 10(c). This confirms that the wireless link stores the power in the magnetic field. The phase response of E and H field is also shown in Fig. 10(b) and (d), respectively. The magnetic field penetrates in the human head, which creates a

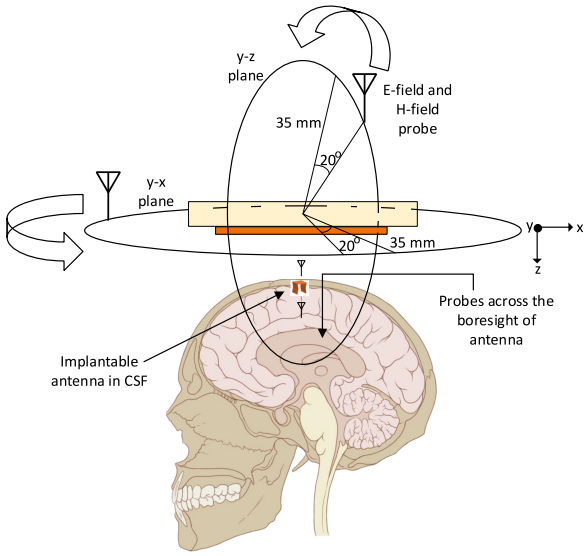

Fig. 9. Near-field simulation of the exterior antenna in the presence of the implantable antenna embedded in the CSF.

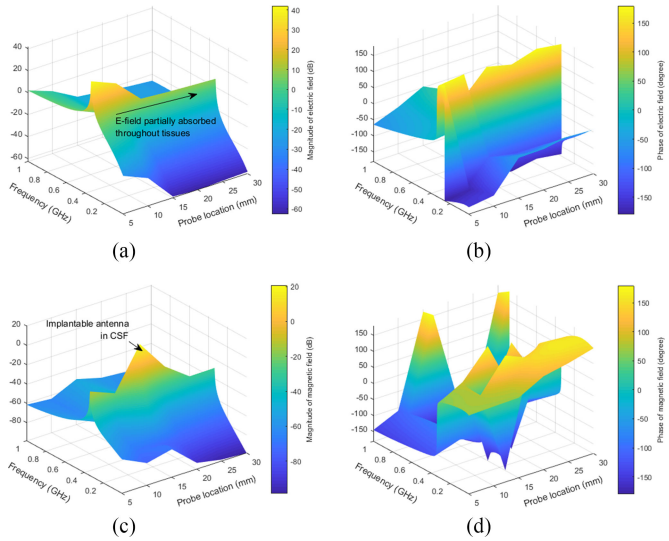

Fig. 10. Near-field penetration in the realistic human head model from the exterior antenna to the implantable antenna immersed in the CSF. (a) Magnitude of the near E field. (b) Phase of the near E field. (c) Magnitude of the near H field. (d) Phase of the near H field.

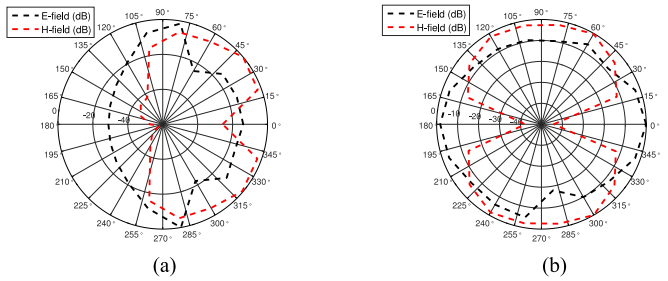

Fig. 11. Near-field radiation pattern of the exterior antenna in the presence of the implantable antenna embedded in the CSF. (a) Radiation pattern of the $y-z$ plane. (b) Radiation pattern of the $y-x$ plane.

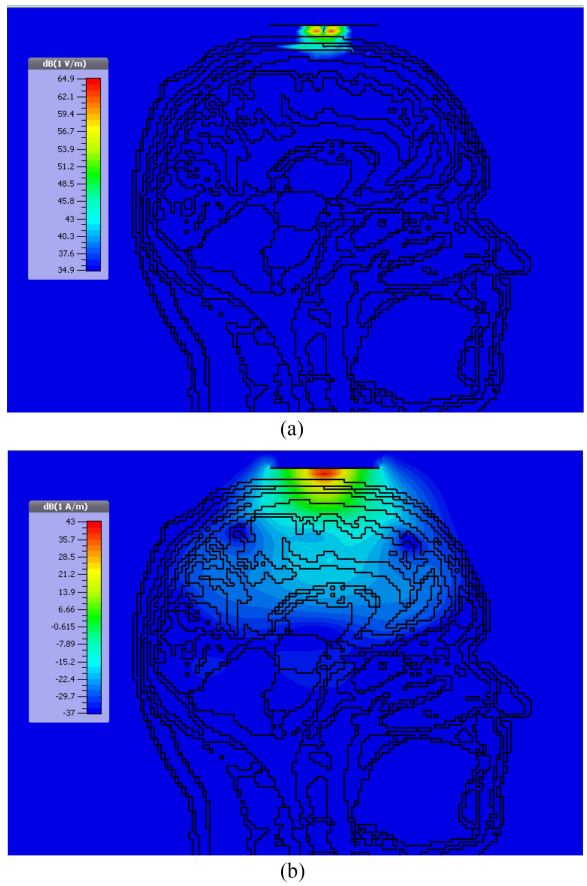

Fig. 12. Near E field and H field penetration in the realistic human head model. (a) Near E field propagation. (b) Near H field propagation.

phase spread for the H field, however, this phase spread does not hold for the E field, which illustrates that the reflection at each tissue interface limits the field propagation in the head along with the tissue absorption of the electric field.

Secondly, probes are placed for $y-z$ and $y-x$ planes at a distance of 35 mm from the center of antenna and then shifted with a resolution of 20^{o} to cover 360^{o} to check the near-field radiation pattern for both planes. The implantable antenna is located in the z-direction of the exterior antenna, from $y-z$ plane, the H and E fields are directional towards the human head model (i.e. z-direction) as shown in Fig. 11.

Sagittal slices of the near E and H field penetration in the realistic human head model are shown in Fig. 12(a) and (b), respectively at 402 MHz, which assert the non-magnetic nature of the biological tissues by storing most of the link power in the magnetic field.

The normalized near E and H fields were also measured in free-space for the exterior antenna located at (0, 0) using near-field probes as shown in Fig. 13. The near-field probes were placed at a distance of 3 cm and scanned a parallel plane of the

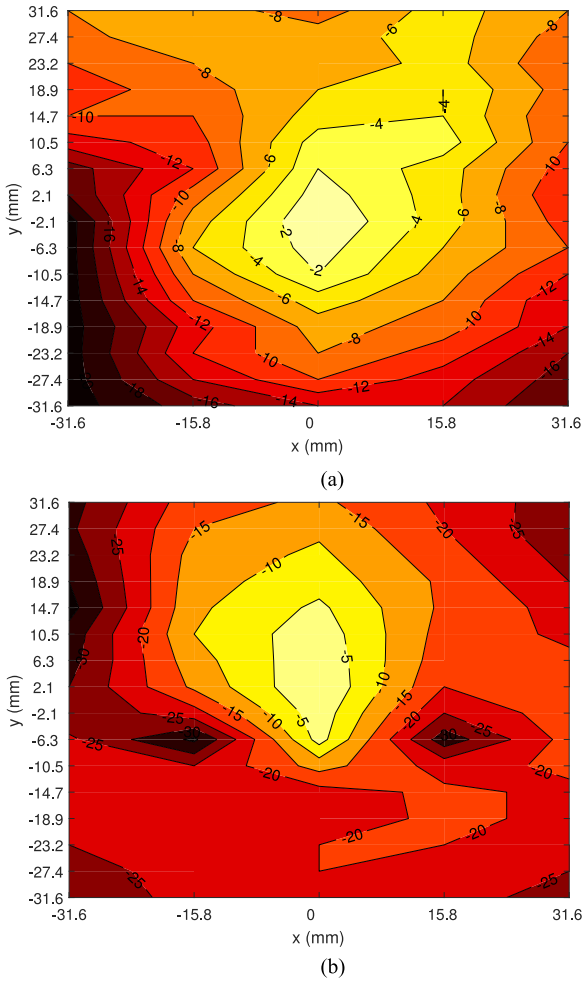

Fig. 13. Measurements of the near (a) E and (b) H fields. The near-field probes were placed at a distance of 3 cm from the exterior antenna in free-space (all values are in dB).

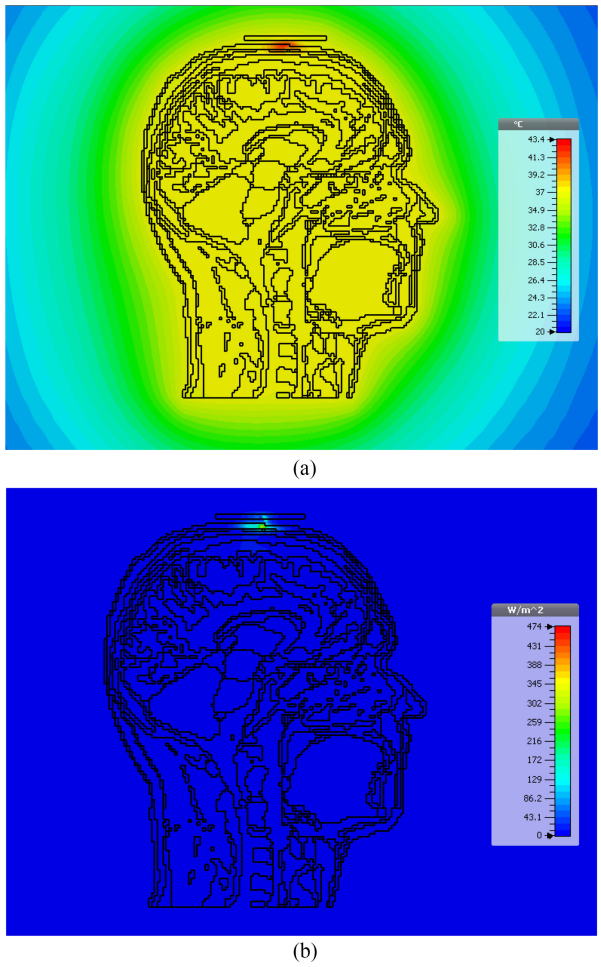

Fig. 14. Thermal simulation of the wireless power link. (a) Temperature distribution. (b) Heat flow density.

exterior antenna as shown in Fig. 13(a) and (b) with a resolution of 15.8 mm in the x-axis and 4.2 mm in the y-axis. The concentration of the fields is within the vicinity of the radiating loop antenna and degrades as the probes move away from the center of the loop. The highest field intensity is achieved when the near-field probe is centrally aligned to the loop antenna. Nevertheless, from the results in Fig. 13, a lateral misalignment of 10 mm in the x-axis and 20 mm in the y-axis for exterior antenna slightly influences the link gain.

VI. Safety Considerations of the Wireless Power Link

A. Specific Absorption Rate

When EM fields propagate through the biological tissues, part of the fields is absorbed and dissipated as heat. The interaction of the EM fields at each tissue interface depends on the operating frequency, dielectric properties of the tissues and whether the exterior antenna is operating in the near or far field. SAR is a measure of the power absorbed by the tissues when exposed to EM fields. This can be described as the time derivative of the incremental energy dW absorbed or dissipated in an incremental dm mass contained in a volume dV of density ρ (kg/m^3) [34]

$$\mathrm{SAR}\left(\frac{W}{kg}\right) = \frac{d}{dt}\left(\frac{dW}{dm}\right) = \frac{d}{dt}\left(\frac{dW}{\rho dV}\right) \tag{6}$$

SAR can also be expressed in terms of the electric field as

$$\mathrm{SAR} = \frac{\sigma}{2\rho}|E|^2 \tag{7}$$

where E (V/m) is the electric field and σ (S/m) is the conductivity. The compliance of the proposed near-field inductive link is investigated with respect to IEEE C95.1-1999 standard ($\mathrm{SAR}_{1g} \leq 1.6$ W/kg) [34] and IEEE C95.1-2005 standard ($\mathrm{SAR}_{10g} \leq 2$ W/kg) [35]. The SAR determines the maximum accepted power to the exterior antenna (P_{in}) as 19 mW to satisfy SAR_{1g} and 82 mW to satisfy SAR_{10g} at 402 MHz. Obtained results of SAR_{1g} in the skin, subcutaneous fat (SAT), skull, CSF, grey matter, white matter and blood are given in Table I. These tissues represent the maximum absorbing tissues among the 46 tissues in the realistic human head model.

TABLE I
SIMULATED MAXIMUM SAR_{1g}, SAR_{10g} GENERATED BY THE EXTERIOR ANTENNA IN THE SKIN, SAT, SKULL, CSF, GREY MATTER, WHITE MATTER AND BLOOD

Tissue	SAR_{1g} (W/kg) for P_{in} = 19 mW	SAR_{10g} (W/kg) for P_{in} = 82 mW
Skin	1.570	1.970
SAT	0.183	0.310
Skull	0.275	0.172
CSF	0.055	0.113
Grey matter	0.046	0.110
White matter	0.028	0.091
Blood	0.182	0.303

B. Temperature Analysis

The absorption of the EM fields by the tissues can cause temperature increase [36], [37], particularly when operating in the near-field. The rate of temperature change in the tissues exposed to EM fields energy is related to SAR as [38]

$$\frac{\triangle T}{\triangle t} = \frac{(\mathrm{SAR} + P_m - P_c - P_b)}{h_c} \tag{8}$$

where $\triangle T$ is the temperature increase ($^{\circ}\mathrm{C}$), $\triangle t$ is the exposure duration time (s), P_m, P_c and P_b are the metabolic heating rate, the rate of heat loss per unit volume due to the thermal conduction and the rate of heat loss per unit volume due to the blood flow, respectively, and h_c is the heat capacity of the tissue ($\mathrm{J/kg}\cdot{}^{o}\mathrm{C}$).

In case of steady-state condition, $P_m = P_c + P_b$, the rate of the temperature rise becomes directly proportional to SAR. Simulations of the temperature analysis is performed through co-simulation between CST Microwave studio with the steady-state thermal solver [30]. The initial body temperature is set as 37 $^{\circ}\mathrm{C}$. Background temperature is considered around 293.1 K. The thermal conductivity and heat capacity have been imported for all tissues from IT'IS foundation online database [31]. The default input power to the exterior antenna port is 1 W. Fig. 14 shows the obtained temperature distribution and the heat flow density from the exterior antenna towards the human head model. From Fig. 14(a), most of the tissues have a temperature around 37 $^{\circ}\mathrm{C}$. However, there is a notable increase in the temperature at the interface of the skin layer. The reason behind this increase is the applied default input power and the skin absorption. In Fig. 15, the power loss per tissue (i.e. volume loss power) is illustrated for the skin, SAT, skull, CSF, grey matter, white matter and blood. It is clearly shown that the skin tissue absorbed 14% from the incident power due to the proximity of the exterior antenna with $d_{ea} = 3$ mm from the skin interface. Hence, the temperature increases in the skin layer. From the SAR analysis in Section VI-A and (8), using 19 mW as an input power to the exterior antenna for SAR_{1g} or 82 mW for SAR_{10g} results in a remarkable reduction in the temperature rise at the skin interface.

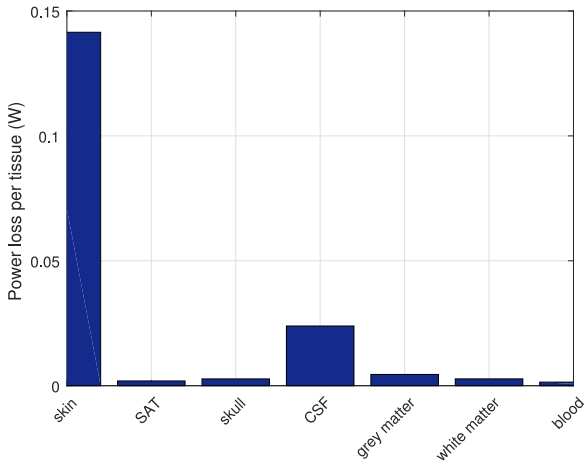

Fig. 15. Absorbed power per tissue with 1 W input power to the exterior antenna (the tissues represent the top five lossy tissues in the human head model).

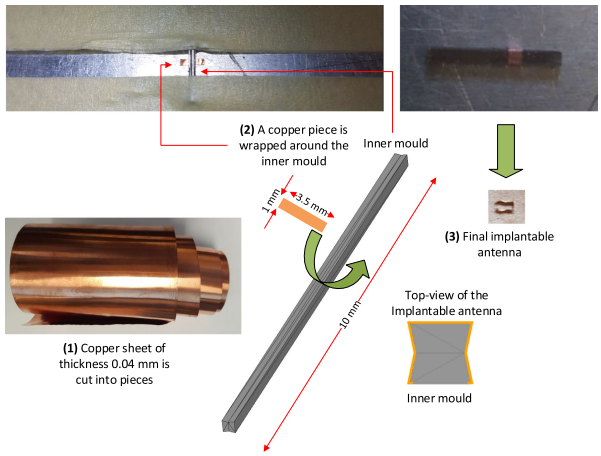

Fig. 16. Fabrication process of the 3D bowtie implantable antenna.

VII. FABRICATION AND IN-VITRO MEASUREMENT RESULTS

The exterior antenna is fabricated on a double-sided copper coated FR4 substrate with 3.2 mm thickness. The loop antenna, matching circuit and balun are on the top side, while, vias connect the ground plane on the rear side with the matching circuit shunt capacitors.

The implantable antenna fabrication procedure is shown in Fig. 16. Firstly, the copper sheet of thickness 0.04 mm is cut into pieces using a paper guillotine into $1 \times 3.5 \times 0.04$ mm^3, then an inner mould is created out of steel with a length of 10 mm to wrap the copper piece around it and finally, the implantable antenna is created, which is soldered to the test board of the same substrate used for the exterior antenna. This fabrication process can be extended to create different shapes of the 3D implantable antenna. Eventually, SMA connectors were soldered to both ends and the capacitors were also connected and soldered accordingly, the final prototypes are shown in Fig. 17.

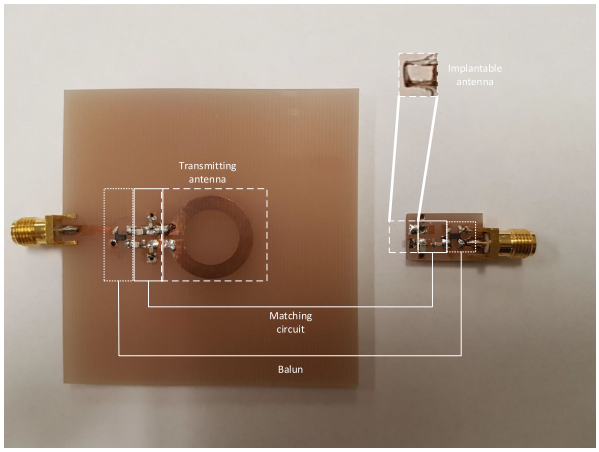

Fig. 17. Prototypes of the exterior antenna and implantable antenna boards connected to a matching circuit and balun.

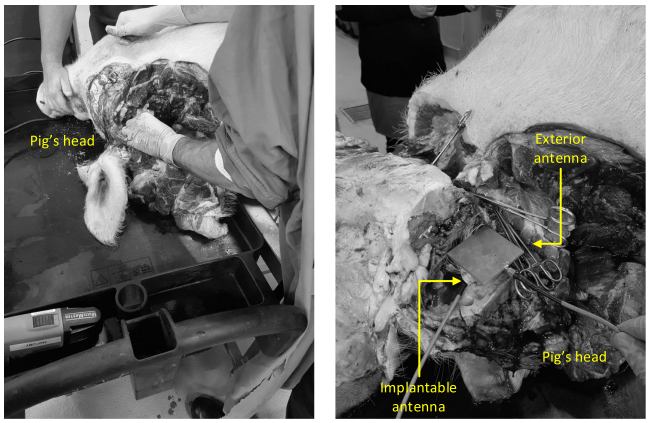

Fig. 18. Measurement of the wireless power link for pig's head: (a) Slicing the pig's head. (b) After placing the implantable and exterior antenna (the images are desaturated due to the blood).

The wireless link gain (1) was tested inside the head of a pig and piglet under the ethical approval from the Animal Ethics Committee of the University of Queensland (ANRFA/ITEE/088/17) to confirm the performance of the designed wireless link in a biological environment. Both the pig and piglet were not euthanized for the purpose of this work as they were obtained from the University of Queensland Gatton Campus Piggery after their death.

Unlike the work in [32], where the skull and brain were removed from the pig's head and the cavity was filled with a head-equivalent liquid phantom, we used more realistic *in-vitro* measurements.

In Fig. 18, the implantable antenna test board was placed over the brain in the CSF, and the exterior antenna was placed at a distance of 3 mm from the skin interface. A pig was used because of the similarity of its dielectric properties to the human. However, its anatomy is different from a human. In particular,

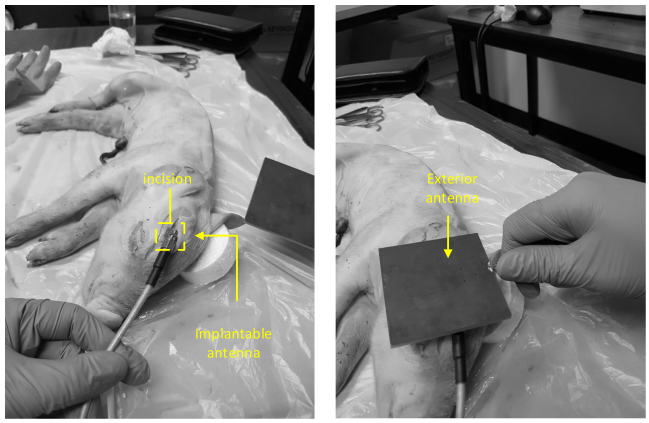

Fig. 19. Measurement of the wireless power link for a piglet: (a) An incision was created in the skull and the implantable antenna was embedded over the brain. (b) After placing the exterior antenna (the images are desaturated due to the blood).

the adult pig's weight was around 250 kg, and the tissue thickness exceeds the human, specifically the skull. Therefore, the skull was sliced to position the test board and then replaced part of the skull, skin and fat on top of the prototype as illustrated in Fig. 18. The measurement in the pig's head was conducted within 30 minutes of its death. Finally, the exterior antenna was placed to verify the wireless link gain. Additionally, the implantable test board was placed in a piglet's head as shown in Fig. 19. An incision was created in the skull and the prototype was placed over the brain as depicted in Fig. 19(a), after that, the exterior antenna was placed at a distance of 3 mm from the skin interface as demonstrated in Fig. 19(b). The piglet was stored in a biospecimen container to avoid temperature and humidity effects on the tissues and the measurement was performed one day after its death.

Fig. 20 shows the measurement results of the wireless link gain in air, pig's head and piglet. In the measurements, G_{op} is characterized based on the power delivered to the load of the implantable antenna from the input power to the matching circuit of the exterior antenna.

Testing in air results in a maximum link gain of -21.44 dB, which is dropped to -35.83 dB inside the pig's head. The loss of the wireless link in the pig's head is implicated in the dielectric properties and the anatomy of the pig's head compared to the case of the human head. In addition, the losses exerted by the cable, mismatch loss between the ports and SMA connectors demonstrate the difference between the simulated and the measured results. Alternatively, testing in the piglet enhanced the link gain to -30.81 dB compared to pig's head measurements as a consequence of the fetal tissues in the piglet. As could be expected, there was a minor frequency shift which was attributed to the discrepancies in the fabrication, measurements and variation in the lumped capacitors with tolerance of 10%. Nevertheless, the measured results of the proposed link show good agreement with the simulation results.

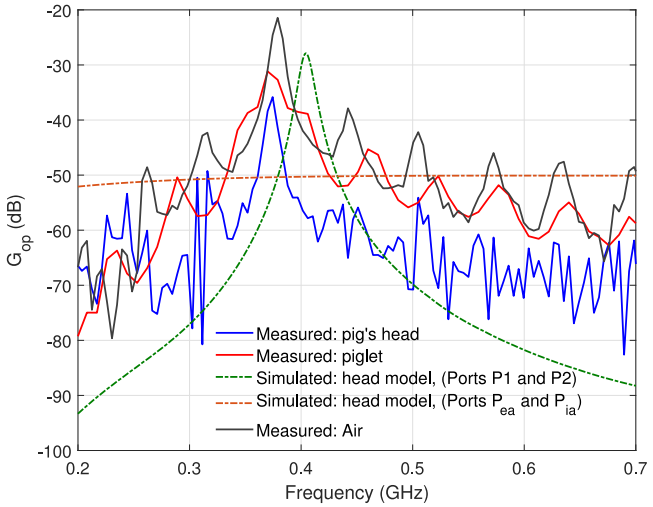

Fig. 20. Measurements and simulation results of the wireless power link gain. In legend, (Ports P1 and P2) refer to the ports in the CST Schematic and (Ports $\mathrm{P_{ea}}$ and $\mathrm{P_{ia}}$) refer to the ports in CST Microwave studio simulation as depicted in Fig. 8.

VIII. Conclusion

An inductive coupling link to power a 3D implantable antenna at MICS band has been presented. The link gain is simulated and optimized in a realistic human head model using a fourth-order Cole-Cole dispersive dielectric properties model. Since, the wireless link is operating in the near-field, the propagation is simulated in the near-field, which demonstrates the efficacy of using an inductive coupling link based on magnetic field. Compliance of the wireless link with the safety requirements has been considered to determine the acceptable power to the exterior antenna and to satisfy the SAR and temperature distribution in the human head model. Using an input power of 19 mW and 82 mW satisfy $\mathrm{SAR_{1g}}$ and $\mathrm{SAR_{10g}}$, respectively. The *in-vitro* measurements of the inductive link between the exterior and 3D implantable antenna with an effective volume of 0.9 $\mathrm{mm^3}$ demonstrate a peak G_{op} of -35.83 dB in pig's head and -30.81 dB in piglet. Hence, the *in-vitro* measurements of the the link gain and the implantable antenna volume provide the best combination for the recent 3D implantable antennas found in the literature.

References

[1] Y. Rahmat-Samii and J. Kim, *Implanted Antennas in Medical Wireless Communications* (Synthesis Lectures on Antennas), vol. 1, no. 1. Williston, VT, USA: Morgan and Claypool Publ., 2006, pp. 1–82.

[2] A. Kiourti and K. S. Nikita, "A review of in-body biotelemetry devices: Implantables, ingestibles, and injectables," *IEEE Trans. Biomed. Eng.*, vol. 64, no. 7, pp. 1422–1430, Jul. 2017.

[3] S. M. Asif *et al.*, "Design and in-vivo test of a batteryless and fully wireless implantable asynchronous pacing system," *IEEE Trans. Biomed. Eng.*, vol. 63, no. 5, pp. 1070–1081, May 2016.

[4] Z. Xiao *et al.*, "An implantable RFID sensor tag toward continuous glucose monitoring," *IEEE J. Biomed. Health Informat.*, vol. 19, no. 3, pp. 910–919, May 2015.

[5] T. Karacolak *et al.*, "Design of a dual-band implantable antenna and development of skin mimicking gels for continuous glucose monitoring," *IEEE Trans. Microw. Theory Tech.*, vol. 56, no. 4, pp. 1001–1008, Apr. 2008.

[6] U. Kawoos *et al.*, "Too much pressure: Wireless intracranial pressure monitoring and its application in traumatic brain injuries," *IEEE Microw. Mag.*, vol. 16, no. 2, pp. 39–53, Mar. 2015.

[7] G. Schalk and E. C. Leuthardt, "Brain-computer interfaces using electrocorticographic signals," *IEEE Rev. Biomed. Eng.*, vol. 4, pp. 140–154, 2011.

[8] A. T. Connolly *et al.*, "A novel lead design for modulation and sensing of deep brain structures," *IEEE Trans. Biomed. Eng.*, vol. 63, no. 1, pp. 148–157, Jan. 2016.

[9] A. Lleo *et al.*, "Cerebrospinal fluid biomarkers in trials for alzheimer and parkinson diseases," *Nat. Rev. Neurol*, vol. 11, no. 1, pp. 41–55, 2015.

[10] H. Mei *et al.*, "Cavity resonator wireless power transfer system for freely moving animal experiments," *IEEE Trans. Biomed. Eng.*, vol. 64, no. 4, pp. 775–785, Apr. 2017.

[11] K. Agarwal, R. Jegadeesan, Y. X. Guo, and N. V. Thakor, "Wireless power transfer strategies for implantable bioelectronics: methodological review," *IEEE Rev. Biomed. Eng.*, vol. PP, no. 99, p. 1, 2017.

[12] A. Waziri *et al.*, "Initial surgical experience with a dense cortical microarray in epileptic patients undergoing craniotomy for subdural electrode implantation," *Neurosurgery*, vol. 64, no. 3, pp. 540–545, 2009, discussion 545.

[13] K. N. Bocan and E. Sejdic, "Adaptive transcutaneous power transfer to implantable devices: A state of the art review," *Sensors*, vol. 16, no. 3, 2016, Art. no. E393.

[14] R. F. Xue *et al.*, "High-efficiency wireless power transfer for biomedical implants by optimal resonant load transformation," *IEEE Trans. Circuits Syst. I, Reg. Papers*, vol. 60, no. 4, pp. 867–874, Apr. 2013.

[15] A. S. Y. Poon *et al.*, "Optimal frequency for wireless power transmission into dispersive tissue," *IEEE Trans. Antennas Propag.*, vol. 58, no. 5, pp. 1739–1750, May 2010.

[16] J. M. Elloian *et al.*, "Continuous wave simulations on the propagation of electromagnetic fields through the human head." *IEEE Trans. Biomed. Eng.*, vol. 61, no. 6, pp. 1676–1683, Jun. 2014.

[17] M. N. Islam and M. R. Yuce, "Review of medical implant communication system (MICS) band and network," *ICT Express*, vol. 2, no. 4, pp. 188–194, 2016.

[18] S. Amendola *et al.*, "Design and optimization of mm-size implantable and wearable on-body antennas for biomedical systems," in *Proc. 2014 8th Eur. Conf. Antennas Propag.*, 2014, pp. 520–524.

[19] L. Song and Y. Rahmat-Samii, "An end-to-end implanted brain-machine interface antenna system performance characterizations and development," *IEEE Trans. Antennas Propag.*, vol. 65, no. 7, pp. 3399–3408, Jul. 2017.

[20] M. Mark *et al.*, "Wireless channel characterization for mm-size neural implants," in *Proc. 2010 Annu. Int. Conf. IEEE Eng. Med. Biol. Soc.*, 2010, pp. 1565–1568.

[21] A. Sani *et al.*, "Antennas and propagation of implanted RFIDs for pervasive healthcare applications," *Proc. IEEE*, vol. 98, no. 9, pp. 1648–1655, Sep. 2010.

[22] M. Manoufali, K. Bialkowski, B. Mohammed, and A. Abbosh, "Wireless power link based on inductive coupling for brain implantable medical devices," *IEEE Antennas Propag. Lett.*, vol. PP, no. 99, 2017.

[23] A. Feriko *et al.*, "Electromagnetic absorption rate in a multilayer human tissue model exposed to base-station radiation using transmission line analysis," *IEEE Antennas Wireless Propag. Lett.*, vol. 13, pp. 903–906, 2014.

[24] R. Lodato *et al.*, "Numerical and experimental characterization of through-the-body UHF-RFID links for passive tags implanted into human limbs," *IEEE Trans. Antennas Propag.*, vol. 62, no. 10, pp. 5298–5306, Oct. 2014.

[25] R. Sarpeshkar, *Ultra Low Power Bioelectronics. Fundamentals, Biomedical Applications, and Bio-inspired Systems*. Cambridge U.K.: Cambridge Univ. Press, 2010.

[26] H. Bahrami *et al.*, "Biological channel modeling and implantable UWB antenna design for neural recording systems," *IEEE Trans. Biomed. Eng.*, vol. 62, no. 1, pp. 88–98, Jan. 2015.

[27] Y. Zhao *et al.*, "Implanted miniaturized antenna for brain computer interface applications: Analysis and design," *PLoS One*, vol. 9, no. 7, 2014, Art. no. e103945.

[28] C. Andreas *et al.*, "The virtual family-development of surface-based anatomical models of two adults and two children for dosimetric simulations," *Phys. Med. Biol.*, vol. 55, no. 2, pp. N23–N38, 2010.

[29] S. Gabriel *et al.*, "The dielectric properties of biological tissues: II. Measurements in the frequency range 10 Hz to 20 GHz," *Phys. Med. Biol.*, vol. 41, no. 11, pp. 2251–2269, 1996.

[30] D. S. Simulia, "Computer Simulation Technology (CST)," 2016.
[31] P. A. Hasgall *et al.*, "IT'IS Database for thermal and electromagnetic parameters of biological tissues, version 3.0," 2015.
[32] E. Moradi *et al.*, "Backscattering neural tags for wireless brain-machine interface systems," *IEEE Trans. Antennas Propag.*, vol. 63, no. 2, pp. 719–726, Feb. 2015.
[33] C. A. Balanis, *Antenna Theory and Analysis*. New York, NY, USA: Wiley, 2005.
[34] *IEEE Standard for Safety Levels With Respect to Human Exposure to Radio Frequency Electromagnetic Fields, 3 kHz to 300 GHz*, IEEE Std C95.1, 1999 Edition, pp. 1–83, 1999.
[35] *IEEE Standard C95.1 for Safety Levels With Respect to Human Exposure to Radio Frequency Electromagnetic Fields, 3 kHz to 300 GHz*, IEEE Std C95.1-2005, 2005.
[36] Y. Zhao *et al.*, "Studies in RF power communication, SAR, and temperature elevation in wireless implantable neural interfaces," *PLoS One*, vol. 8, no. 11, 2013, Art. no. e77759.
[37] H. N. Schwerdt *et al.*, "Analysis of electromagnetic fields induced in operation of a wireless fully passive backscattering neurorecording microsystem in emulated human head tissue," *IEEE Trans. Microw. Theory Techn.*, vol. 61, no. 5, pp. 2170–2176, May 2013.
[38] A. V. Vorst *et al.*, *RF/Microwave Interaction With Biological Tissues*. New York, NY, USA: Wiley, 2006.